



Quantum phases of Rydberg atoms on a kagome lattice

Rhine Samajdar^{a,1} , Wen Wei Ho^{a,b} , Hannes Pichler^{c,d}, Mikhail D. Lukin^a, and Subir Sachdev^{a,1}

^aDepartment of Physics, Harvard University, Cambridge, MA 02138; ^bDepartment of Physics, Stanford University, Stanford, CA 94305; ^cInstitute for Theoretical Physics, University of Innsbruck, Innsbruck A-6020, Austria; and ^dInstitute for Quantum Optics and Quantum Information, Austrian Academy of Sciences, Innsbruck A-6020, Austria

Contributed by Subir Sachdev, November 25, 2020 (sent for review July 29, 2020; reviewed by Subhro Bhattacharjee and Arun Paramakanti)

We analyze the zero-temperature phases of an array of neutral atoms on the kagome lattice, interacting via laser excitation to atomic Rydberg states. Density-matrix renormalization group calculations reveal the presence of a wide variety of complex solid phases with broken lattice symmetries. In addition, we identify a regime with dense Rydberg excitations that has a large entanglement entropy and no local order parameter associated with lattice symmetries. From a mapping to the triangular lattice quantum dimer model, and theories of quantum phase transitions out of the proximate solid phases, we argue that this regime could contain one or more phases with topological order. Our results provide the foundation for theoretical and experimental explorations of crystalline and liquid states using programmable quantum simulators based on Rydberg atom arrays.

Rydberg quantum simulators | density-wave orders | quantum phase transitions

The search for quantum phases with fractionalization, emergent gauge fields, and anyonic excitations has been a central focus of research in quantum matter for the past three decades (1, 2). Such systems feature long-range many-body quantum entanglement, which can, in principle, be exploited for fault-tolerant quantum computing (3). The best-studied examples in this regard are the fractional quantum Hall states found in high magnetic fields (4). While such states have, by now, been realized in a wide variety of experimental systems, their intrinsic topological properties, including anyonic statistics, are challenging to detect and control directly (5). In the absence of a magnetic field, the simplest anyonic phase compatible with time-reversal symmetry is the so-called \mathbb{Z}_2 spin liquid (6, 7), which has the same topological order as the “toric code” (3). While there are some indications that such a phase may be present in electronic systems on the kagome lattice (8–10), thus far, these quantum spin liquid (QSL) states have evaded direct experimental detection.

In the search for QSLs, systems with frustration (11, 12)—which can be either of geometric origin or induced by further-neighbor couplings—constitute a promising avenue of exploration. Motivated by this consideration, here, we investigate many-body states of neutral atom arrays, interacting via laser excitation to atomic Rydberg states (13), that have been found to display a variety of interesting correlated quantum phases in one and two dimensions (14–20). Specifically, we examine a realistic model of Rydberg atoms on the kagome lattice and perform density-matrix renormalization group (DMRG) computations to establish its rich phase diagram as a function of laser parameters and atomic distances. These calculations reveal the formation of several intricate solid phases with long-range density-wave order. We show that one of these ordered phases actually emerges from a highly degenerate manifold of classical states via a quantum order-by-disorder mechanism. We also find a strongly correlated “liquid regime” of parameter space (identified by the star in Fig. 1E) where the density of Rydberg excitations is limited by the interactions, in contrast to the gas-like “disordered regime” where the laser driving induces independent atomic

excitations. While for most interaction strengths solid phases appear in such a dense regime, we observe that the liquid regime has no local order and significant entanglement entropy. We employ a mapping to the triangular lattice quantum dimer model (21), which correctly describes the solid phases proximate to the liquid regime in the Rydberg model. Theories for quantum phase transitions out of these solid phases then imply that part of this liquid regime hosts states with long-range topological order. While our numerical results do not provide direct evidence for topological order over the system sizes studied, we demonstrate that this regime should be readily accessible in experiments, raising the possibility of experimental investigations of entangled quantum matter. Remarkably, this is made possible simply by using appropriate lattice geometries and innate interactions, even without carefully engineering specific gauge constraints (22).

Kagome Lattice Rydberg Model

Our interest lies in studying the phases of neutral atoms arranged on a kagome lattice, as sketched in Fig. 1A. Each kagome unit cell comprises three sites on a triangular scaffolding and the primitive vectors of this lattice are $\mathbf{a}_1 = (2a, 0)$ and $\mathbf{a}_2 = (a, \sqrt{3}a)$, where the lattice constant a is the spacing between two nearest-neighboring sites. Let us denote the number of complete unit cells along \mathbf{a}_μ by N_μ . In a minimal model, each atom can be regarded as a two-level system with $|g\rangle_i$ and $|r\rangle_i$ representing the internal ground state and a highly excited Rydberg state of

Significance

Programmable quantum simulators based on Rydberg atom arrays have recently emerged as versatile platforms for exploring exotic many-body phases and quantum dynamics of strongly correlated systems. In this work, we theoretically investigate the quantum phases that can be realized by arranging such Rydberg atoms on a kagome lattice. Along with an extensive analysis of the states which break lattice symmetries due to classical correlations, we identify an intriguing regime that constitutes a promising candidate for hosting a phase with long-range quantum entanglement and topological order. Our results provide a route to experimentally realizing and probing highly entangled quantum matter.

Author contributions: R.S. and S.S. designed research; R.S., W.W.H., H.P., M.D.L., and S.S. performed research; R.S., W.W.H., H.P., M.D.L., and S.S. analyzed data; and R.S., W.W.H., H.P., M.D.L., and S.S. wrote the paper.

Reviewers: S.B., International Centre for Theoretical Sciences; and A.P., University of Toronto.

The authors declare no competing interest.

Published under the PNAS license.

¹To whom correspondence may be addressed. Email: sachdev@g.harvard.edu or rhine.samajdar@g.harvard.edu.

This article contains supporting information online at <https://www.pnas.org/lookup/suppl/doi:10.1073/pnas.2015785118/-DCSupplemental>.

Published January 18, 2021.

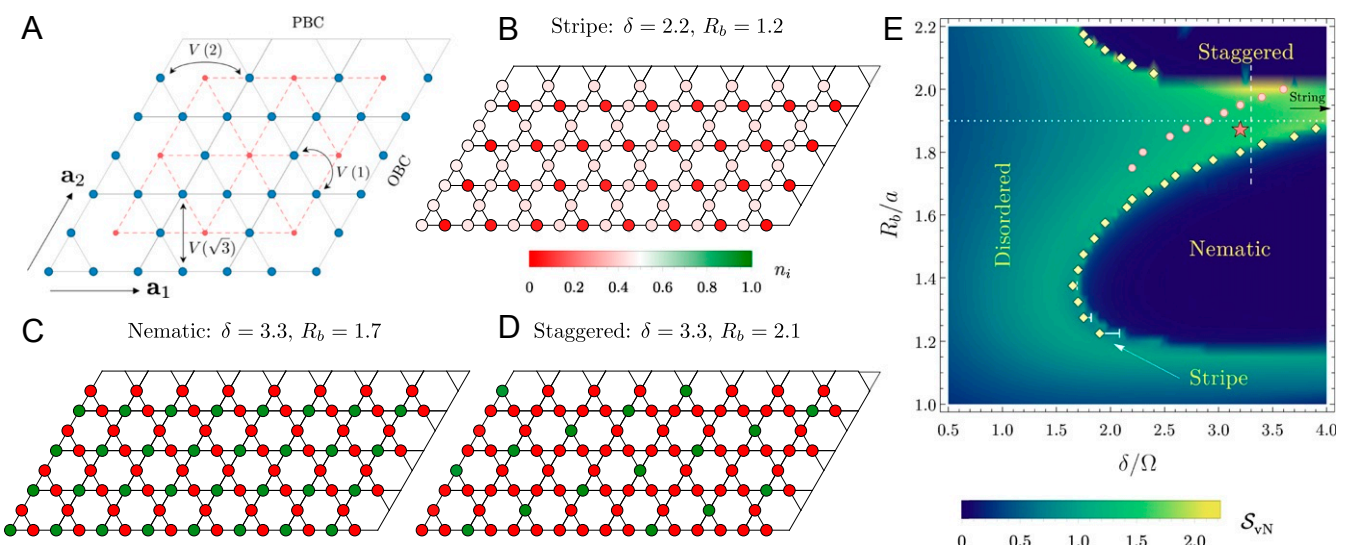


Fig. 1. Phases of the kagome lattice Rydberg atom array. (A) Geometry of the kagome lattice. The lattice vectors are $\mathbf{a}_1 = (2, 0)$, $\mathbf{a}_2 = (1, \sqrt{3})$. Periodic boundary conditions (PBC) and open boundary conditions (OBC) are imposed along the \mathbf{a}_2 and \mathbf{a}_1 directions, resulting in a cylinder. The blue dots are the sites of the original kagome lattice, where the atoms reside, while the red dots outline the medial triangular lattice formed by connecting the centers of the kagome hexagons. (B–D) The various possible symmetry-broken ordered phases. Each lattice site is color coded such that green (red) signifies the atom on that site being in the Rydberg (ground) state. (E) Phase diagram of the Hamiltonian (1) in the δ – R_b plane. The yellow diamonds and pink circles are determined from the maxima of the susceptibility at each R_b ; the former correspond to the finite-size pseudocritical points delineating the boundaries of the ordered phases. The white bars delimit the extent of the stripe phase. The string phase (Fig. 2) lies at larger detuning, beyond the extent of this phase diagram, as conveyed by the black arrow. The correlated liquid regime is marked by a red star. The cuts along the dotted and dashed lines are analyzed in Figs. 5 and 7, respectively.

the i th atom. The system is driven by a coherent laser field, characterized by a Rabi frequency, Ω , and a detuning, δ . Putting these terms together, and taking into account the interactions between atoms in Rydberg states (23), we arrive at the Hamiltonian

$$H_{\text{Ryd}} = \sum_{i=1}^N \frac{\Omega}{2} (|g\rangle_i \langle r| + |r\rangle_i \langle g|) - \delta |r\rangle_i \langle r| + \frac{1}{2} \sum_{(i,j)} V(|\mathbf{x}_i - \mathbf{x}_j|/a) |r\rangle_i \langle r| \otimes |r\rangle_j \langle r|, \quad [1]$$

where the integers i, j label sites (at positions $\mathbf{x}_{i,j}$) of the lattice, and the repulsive interaction potential is of the van der Waals form $V(R) = C/R^6$ (24). Crucially, the presence of these interactions modifies the excitation dynamics. A central role in the physics of this setup is played by the phenomenon of the Rydberg blockade (25, 26) in which strong nearest-neighbor interactions ($V(1) \gg |\Omega|, |\delta|$) can effectively prevent two neighboring atoms from simultaneously being in Rydberg states. The excitation of one atom thus inhibits that of another and the associated sites are said to be blockaded. By reducing the lattice spacing a , sites spaced farther apart can be blockaded as well and it is therefore convenient to parameterize H_{Ryd} by the “blockade radius,” defined by the condition $V(R_b/a) \equiv \Omega$ or equivalently, $C \equiv \Omega R_b^6$. Finally, we recognize that by identifying $|g\rangle$, $|r\rangle$ with the two states of a $S = 1/2$ spin, H_{Ryd} can also be written as a quantum Ising spin model with C/R^6 interactions in the presence of longitudinal (δ) and transverse (Ω) fields (27).

We determine the quantum ground states of H_{Ryd} for different values of δ/Ω and R_b/a using the DMRG (28, 29), which has been extensively employed on the kagome lattice to identify both magnetically ordered and spin liquid ground states of the antiferromagnetic Heisenberg model (30–32). The technical aspects of our numerics are documented in *SI Appendix, section I*. In particular, we work in the variational space spanned

by matrix product state (MPS) ansätze of bond dimensions up to $d = 3,200$. Although (i, j) runs over all possible pairs of sites in Eq. 1, this range is truncated in our computations, where we retain interactions between atoms separated by up to $2a$ (third-nearest neighbors), as shown in Fig. 1A. To mitigate the effects of the boundaries, we place the system on a cylindrical geometry by imposing open (periodic) boundary conditions along the longer (shorter) \mathbf{a}_1 (\mathbf{a}_2) direction. The resulting cylinders are labeled by the direction of periodicity and the number of sites along the circumference; for instance, Fig. 1A depicts a YC6 cylinder. Since the computational cost of the algorithm (for a constant accuracy) scales exponentially with the width of the cylinder (33), here, we limit the systems considered to a maximum circumference of 12 lattice spacings. Unless specified otherwise, we always choose the linear dimensions N_1, N_2 to yield an aspect ratio of $N_1/N_2 \simeq 2$, which is known to minimize finite-size corrections and optimize DMRG results in two dimensions (34, 35).

Phase Diagram

We first list the various phases of the Rydberg Hamiltonian that can arise on the kagome lattice. Without loss of generality, we set $\Omega = a = 1$ hereafter for notational convenience. At large negative detuning, it is energetically favorable for the system to have all atoms in the state $|g\rangle$, corresponding to a trivial “disordered” phase with no broken symmetries (36). As δ/Ω is tuned toward large positive values, the fraction of atoms in $|r\rangle$ increases but the geometric arrangement of the excitations is subject to the constraints stemming from the interactions between nearby Rydberg atoms. This competition between the detuning and the previously identified blockade mechanism results in so-called “Rydberg crystals” (37), in which Rydberg excitations are arranged regularly across the array, engendering symmetry-broken density-wave ordered phases (19). On the kagome lattice, the simplest such crystal that can be formed—while respecting the blockade restrictions—is constructed by having an atom in the excited state on exactly one out of the three sublattices in the kagome unit cell. This is the ordering pattern of the “nematic”

phase (Fig. 1C), which is found in a regime where only nearest-neighbor sites are blockaded. The nematic order spontaneously breaks the threefold rotational (C_3) symmetry of the underlying kagome lattice, so, for an infinite system, the true ground state is triply degenerate within this phase. Even though H_{Ryd} does not conserve the number of Rydberg excitations, the ordered state can still be characterized by a “filling fraction” upon taking the classical limit $\delta/\Omega \rightarrow \infty$, $R_b/a \neq 0$, which, in this case, leads to a density of $\langle n_i \rangle = 1/3$, where $n_i \equiv |\langle r \rangle_i \langle r |$.

Curiously, the nematic phase is separated from the trivial disordered one by a sliver of a quantum solid without any classical analogue, to wit, the stripe phase seen in Fig. 1B. This state also breaks the C_3 symmetry; accordingly, between the disordered and stripe phases, one encounters a \mathbb{Z}_3 -symmetry-breaking quantum phase transition (QPT) (38) in the universality class of the (2 + 1)D three-state Potts model (39), while the QPT demarcating stripe and nematic is first order. Although both phases break the same symmetry, the stripe ordering is distinguished from the nematic by a substantial and equal density on two sublattices of the unit cell. The formation of these stripes can be attributed to quantum fluctuations (19), which help stabilize the phase in a narrow window as follows. The system optimizes the geometric packing in a configuration where all atoms on one sublattice are in the ground state, whereas those on the other two sublattices are each in a quantum superposition formed by the ground state with a coherent admixture of the Rydberg state. These “dressed” atoms assist in offsetting the energetic penalty due to the interactions, while simultaneously maximizing the excitation density and therefore the reduction in energy from δ . The ensuant average density in the stripe phase is also $\langle n_i \rangle \sim 1/3$, which explains its existence as a precursor to the nematic ordering. The extent of this phase narrows significantly with increasing R_b , so it is difficult to ascertain whether the transition between the lattice nematic and disordered phases is always a two-step one with the stripe order intervening. Nevertheless, based on our current data (see Fig. 7), we believe it is likely that the stripe phase terminates at a tricritical point near the tip of the nematic dome instead of surrounding it throughout.

Proceeding to larger blockade radii, we find that the kagome Rydberg array hosts yet another solid phase with density-wave ordering, namely the “staggered” phase (Fig. 1D). This phase, which bears a 12-fold ground-state degeneracy, is realized when interactions between neighboring Rydberg atoms are sufficiently strong enough to blockade third-nearest-neighbor sites, so the excitations are positioned a distance of $\sqrt{7}$ apart. The resultant Rydberg crystals are formed of a 12-site unit cell with lattice vectors $4\mathbf{a}_1$ and $2\mathbf{a}_1 + \mathbf{a}_2$; the associated classical density is 1/6. The staggered phase remains stable up to $R_b \lesssim \sqrt{7}$, beyond which fourth-nearest neighbors are also blockaded.

Equipped with the information above, we now turn to assembling the full phase diagram of H_{Ryd} . An unbiased diagnostic to do so is the bipartite von Neumann entanglement entropy (EE) of the ground state $S_{\text{vN}} \equiv -\text{Tr}(\rho_r \ln \rho_r)$, ρ_r being the reduced density matrix for each subsystem when the cylinder is partitioned in half along \mathbf{a}_1 . On going from the disordered phase to an ordered one, S_{vN} gradually increases, peaks near the quantum critical point (QCP), and then drops sharply inside the solid phase (see Fig. 5C). This is because the DMRG prefers states with low entanglement and systematically converges to a so-called minimal entropy state (MES) (35, 40), which is simply one of the symmetry-broken states rather than their superposition. This drastic decline in S_{vN} traces out the two lobes seen in Fig. 1E, which mark the phase boundaries of the nematic and staggered orders. In the limit of large detuning, there is another density-wave ordered phase between these two lobes, which we christen the “string” phase and discuss next.

Quantum Order by Disorder

In the classical limit of $\delta/\Omega \rightarrow \infty$, the periodic arrangement of Rydberg excitations (or equivalently hard-core bosons) on the kagome lattice can result in additional ordered phases besides the nematic and the staggered ones at various fractional densities (41). To see this, one can simply minimize the classical energy, which is determined solely by the competition between the detuning and the repulsive interactions. In the parameter range of interest ($R_b \lesssim 2.25$), it is not difficult to observe (Fig. 2D) that this optimization yields three regions characterized by classical filling fractions of

$$f = \begin{cases} 1/3; & V_3/\delta < 1/7, \\ 2/9; & 1/7 < V_3/\delta < 1/4, \\ 1/6; & 1/4 < V_3/\delta, \end{cases} \quad [2]$$

where V_3 represents the strength of the third-nearest-neighbor interactions. Since we have (temporarily) set $\Omega = 0$, the ratio V_3/δ is the only independent tuning parameter for the Hamiltonian in this limit.

The phases at fillings of a third and a sixth can be readily identified as (the classical versions of) the familiar nematic and staggered orders (Fig. 1C and D), respectively. In between the two, the system favors a separate highly degenerate classical ground state, forming what we dub the string phase. A few of the possible ordering patterns for a crystal belonging to this phase, with a filling fraction of $f = 2/9$, are presented in Fig. 2 A–C. The arrangement of the Rydberg excitations resembles strings—which may be straight or bent—that stretch across the lattice. Interestingly, there are a macroscopic number of such states, all with the same classical energy, and this degeneracy grows

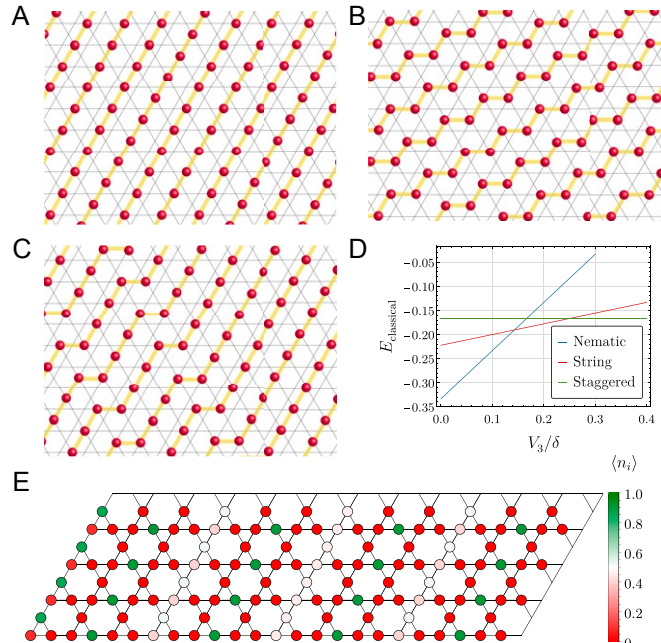


Fig. 2. Crystalline phase at 2/9 filling on the kagome lattice. (A–C) Classically ordered states at $f = 2/9$. While we sketch only three configurations here, the number of such states—with the same filling fraction—scales exponentially with the system size. The Rydberg excitations (red) are arranged in “strings” (yellow) that span the lattice. (D) Comparing the three possible classical phases, we find that the energy (at $\Omega = 0$) is minimized by the string-ordered state over a finite region between the nematic and the staggered phases. (E) Rydberg crystal formed in the string phase at $\delta = 4.00$, $R_b = 1.95$ on a wide ($N_1 = 12$) YC8 cylinder.

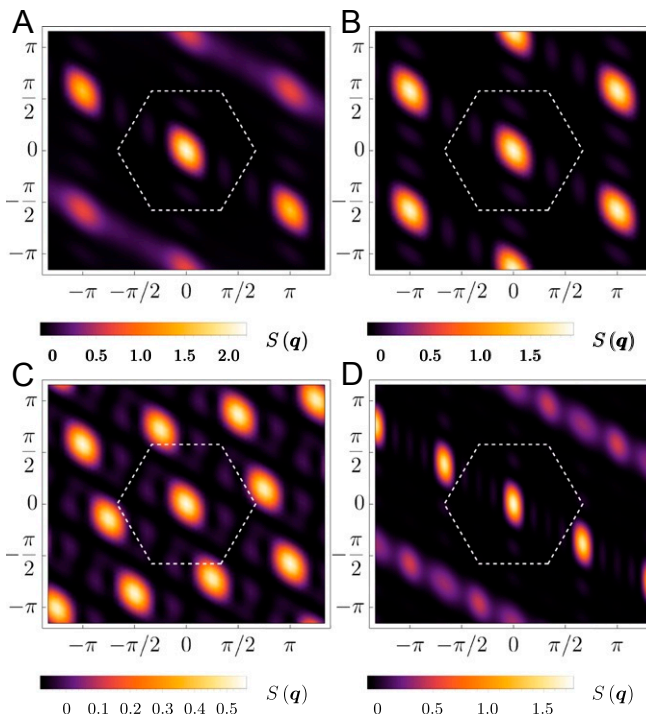


Fig. 3. Static structure factors of the various ordered phases. $S(\mathbf{q})$ displays pronounced and well-defined peaks for the (A) stripe ($\delta = 2.20$, $R_b = 1.20$), (B) nematic ($\delta = 3.30$, $R_b = 1.70$), (C) staggered ($\delta = 3.30$, $R_b = 2.10$), and (D) string ($\delta = 4.00$, $R_b = 1.95$) orders. The dashed white hexagon marks the first Brillouin zone of the kagome lattice. The structure factor for the string phase is computed on the cylindrical geometry shown in Fig. 2E.

exponentially with the linear dimensions of the system. For example, in Fig. 2A, the positions of all of the atoms in the Rydberg state can be uniformly shifted by $\pm \mathbf{a}_2/2$ for every other string without affecting the energy, leading to $\mathcal{O}(2^{N_1})$ potential configurations. Similarly, when the strings are bent, like in Fig. 2C, there are $\mathcal{O}(N_2)$ locations where a kink can be formed and, correspondingly, $\mathcal{O}(2^{N_2})$ states of this type.

The large classical degeneracy raises the question of the fate of this phase once we reinstate a nonzero transverse field, Ω . There are two natural outcomes to consider. First, a superposition of the classical ground states can form a quantum liquid with topological order, as is commonly seen to occur in quantum dimer models (42). However, a necessary condition in this regard is the existence of a local operator which can connect one classical ground state with another. Since the individual ground states are made up of parallel strings, they are macroscopically far away from each other, and it would take an operator with support of the size of the system length to move between different classical configurations, thus violating the requirement of locality. This brings us to the second possibility, namely, that a quantum “order-by-disorder” phenomenon (43, 44) prevails. In this mechanism, quantum fluctuations lower the energy of particular classical states in the degenerate manifold; the system then orders in a state around which the cost of excitations is especially cheap. In this case, one could anticipate a string-ordered solid phase, which should be easily identifiable from the structure factor.

The DMRG numerics confirm our intuition that such a crystal should emerge in the phase diagram at sufficiently high detunings. On the YC8 cylinder with $N_1 = 8$, the string phase appears at detunings beyond the range rendered in Fig. 1E. However, it is manifestly observed, for a wider geometry, in

Fig. 2E, which illustrates the local magnetizations inside the string phase (at $\delta = 4.00$, $R_b = 1.95$) on a YC8 cylinder of length $N_1 = 12$ (chosen to be fully compatible with the string order). The ground state found by finite DMRG is patently ordered with the system favoring a configuration of straight strings that wrap around the cylinder, thereby lifting the macroscopic classical degeneracy. This is in contrast to the expectation from naive second-order perturbation theory, which picks out the maximally kinked classical state.

Signatures of Density-Wave Orders

In totality, we have thus detected four solid phases on the kagome lattice. All these ordered states can be identified from either their respective structure factors or the relevant order parameters, as we now show.

With a view to extracting bulk properties, in the following, we work with the central half of the system that has an effective size of $N_c = 3N_2^2$. Evidence for ordering or the lack thereof can be gleaned from the static structure factor, which is the Fourier transform of the instantaneous real-space correlation function

$$S(\mathbf{q}) = \frac{1}{N_c} \sum_{i,j} e^{i\mathbf{q} \cdot (\mathbf{x}_i - \mathbf{x}_j)} \langle n_i n_j \rangle \quad [3]$$

with the site indexes i, j restricted to the central $N_2 \times N_2$ region of the cylinder. At a blockade radius of $R_b = 1.7$, which stations one in the nematic phase (Fig. 3B), the structure factor has pronounced maxima at the corners of the (hexagonal) extended Brillouin zone, occurring at $\mathbf{Q} = \pm \mathbf{b}_1, \pm \mathbf{b}_2, \pm (\mathbf{b}_1 + \mathbf{b}_2)$, where $\mathbf{b}_1 = (\pi, -\pi/\sqrt{3})$ and $\mathbf{b}_2 = (0, 2\pi/\sqrt{3})$ are the reciprocal lattice vectors. A subset of these maxima also persists for the stripe phase (Fig. 3A)—this is in distinction to the nematic phase wherein the peaks at all six reciprocal lattice vectors are of equal strength. In the presence of staggered ordering (Fig. 3C), the peaks are comparatively weaker but prominent nonetheless, appearing at $\mathbf{Q} = \pm \mathbf{b}_1, \pm (\pi/2, \sqrt{3}\pi/2), \pm (3\pi/4, \pi/(4\sqrt{3}))$, and $\pm (-\pi/4, 5\pi/(4\sqrt{3}))$. Likewise, in the string phase (Fig. 3D), conspicuous maxima are seen to occur at $\pm 2\mathbf{b}_1/3$ for the ground-state configuration where straight strings encircle the lattice. While we list here the ordering wavevectors for a finite system, let us briefly note that on an infinite lattice, the structure factors, of course, would additionally include C_3 -rotated copies of the above.

One can also directly look at the order parameters that diagnose the possible symmetry-broken ordered states. For the nematic phase, an appropriate definition is

$$\Phi = \frac{3}{N_c} \left(\sum_{i \in A} n_i + \omega \sum_{i \in B} n_i + \omega^2 \sum_{i \in C} n_i \right),$$

where $\omega \equiv \exp(2\pi i/3)$ is the cube root of unity, and A, B, C denote the three sublattices of the kagome lattice. Similarly, in the staggered and string phases, one can define the (squared) magnetic order parameter $M_Q^2 \equiv S(\mathbf{Q})$, with \mathbf{Q} chosen from among the observed peaks of the structure factor. These order parameters are more quantitatively addressed (see Fig. 7A, which catalogs the ground-state properties calculated at a fixed detuning of $\delta = 3.3$ [dashed line in Fig. 1E]; in particular, we observe that the nematic and staggered order parameters assume nontrivial values in exactly the regions predicted by the phase diagram.)

Mapping to Triangular Lattice Quantum Dimer Models

At large detuning, we can approximately map the Rydberg system to a model of hard-core bosons at filling f on the kagome lattice. The bosonic system (21, 45–49) has an extra U(1) symmetry, which can be spontaneously broken in a superfluid phase;

in the Rydberg model without the $U(1)$ symmetry, the disordered phase is the counterpart of the superfluid. However, any nonsuperfluid topological states of the boson model are insensitive to the $U(1)$ symmetry and can also be present in the Rydberg model.

In the limit of strong interactions, hard-core bosons at filling $f = (1/2, 1/3, 1/6)$ on the kagome lattice map (21, 45–47) onto an (odd, even, odd) quantum dimer model (QDM) (50–52) on the medial triangular lattice with $N_d = (3, 2, 1)$ dimers per site, with odd/even referring to the parity of N_d . The triangular lattice of the QDM is formed by joining the centers of the kagome hexagons, and this correspondence is sketched in Fig. 4, which schematically shows the mapping between the different Rydberg solids and the phases of the QDM. A key observation here is that both solid phases next to the liquid regime (marked by the star in Fig. 1E) are also phases of the QDM: The nematic phase was found in the QDM with $N_d = 2$ by Roychowdhury et al. (21), and the staggered phase is present in the QDM with $N_d = 1$ (50, 51). In both cases, a \mathbb{Z}_2 spin liquid phase with topological order has been found adjacent to these solid phases (21, 50, 51) in the QDMs. Making the reasonable assumption that a QDM description for the Rydberg system holds in the vicinity of the phase boundaries of these solid states, we expect \mathbb{Z}_2 topological order in the liquid regime of the Rydberg model in Fig. 1, proximate to the nematic and staggered solid phases.

There is a subtle difference between the \mathbb{Z}_2 spin liquids found in the $N_d = 1, 2$ QDMs: The anyonic “vison” excitation picks up a Berry phase of π (2π) upon adiabatic transport around a site of an odd (even) QDM (2, 50, 51, 53–60). This distinction changes the projective symmetry group of the visons and also holds for the \mathbb{Z}_2 spin liquids expected in the Rydberg model, which must therefore be odd/even as well. Consequently, the spin liquids proposed to be proximate to the staggered and nematic phases are not identical; one or both of them could be present in the liquid regime. Moreover, the vison Berry phase places important constraints on the nontopological states obtained by condensing visons: For instance, an odd \mathbb{Z}_2 spin liquid cannot have a vison-condensing phase transition to a trivial disordered state with no broken lattice symmetry, which is a manifestation of the Lieb–Schultz–Mattis theorem.

Roychowdhury et al. (21) studied the transition from the even \mathbb{Z}_2 spin liquid into the nematic phase. The visons in this \mathbb{Z}_2 spin liquid have an energy dispersion with minima at $\mathbf{M}_1 = (\pi/2, -\pi/(2\sqrt{3})) = \mathbf{b}_1/2, \mathbf{M}_2 = (0, \pi/\sqrt{3}) = \mathbf{b}_2/2$ (21), and their condensation leads to the nematic ordering for which the dominant wavevectors are $\mathbf{b}_1, \mathbf{b}_2$ (Fig. 3B). The critical theory for this transition is an $O(3)$ Wilson–Fisher theory with cubic anisotropy (21), and this conclusion holds for both the QDM and the Rydberg system. It is interesting to compare this result to that for the transition from the nematic phase to the disordered phase of the Rydberg model, which was mentioned above to be in the universality class of the $(2 + 1)$ D three-state Potts model and hence, weakly first order (39). Therefore, the nematic phase can melt either by a first-order transition to a trivial disordered phase or via a second-order one into a topological phase by fractionalizing the nematic order parameter. So, the observation of a continuous $O(3)$ transition out of the nematic phase to a phase without symmetry breaking would constitute nontrivial evidence for the presence of \mathbb{Z}_2 topological order in the latter. An apparent second-order transition in the nematic order parameter can be seen (see Fig. 7B), although our numerical accuracy is not sufficient to determine its universality class.

The transition from the staggered phase to the odd \mathbb{Z}_2 spin liquid of the $N_d = 1$ QDM is first order (50, 51), and we expect it to be so for the Rydberg model too. This is compatible with the rapid increase of the staggered order parameter out of the liquid

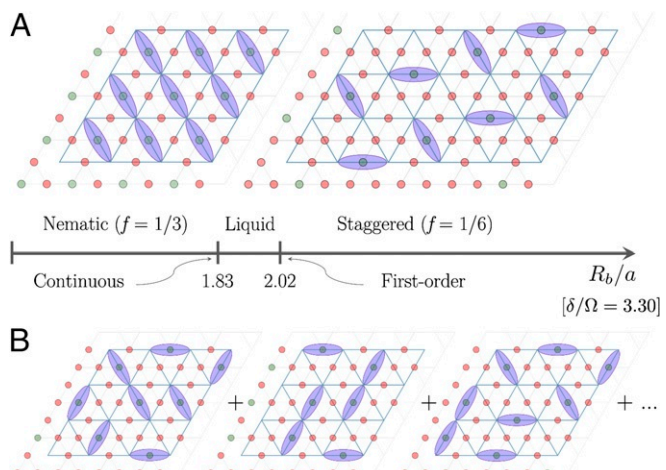


Fig. 4. Correspondence between the Rydberg and quantum dimer models. In the limit of large detuning, the Rydberg excitations can be mapped to a system of hard-core bosons, upon identifying each atom in state $|r\rangle$ ($|g\rangle$) as an occupied (empty) bosonic mode (27). (A) The resultant boson model is at a filling of $f = 1/3$ ($1/6$) for the nematic (staggered) phase. A boson on any site of the kagome lattice (red/green points) can now be uniquely associated with a dimer on the corresponding bond of the medial triangular lattice (blue lines) (21). The liquid regime is separated from the nematic (staggered) phase by a continuous (first-order) QPT. (B) Schematic depiction of a potential Rydberg liquid as a superposition of dimer configurations. Note that, unlike in the QDM, the total number of dimers can fluctuate in the Rydberg model.

regime (see Fig. 7B). We also note that the density of Rydberg excitations in the liquid regime (~ 0.2) is close to that of the odd QDM ($f = 1/6$).

For both the even and odd \mathbb{Z}_2 spin liquids proposed for the liquid regime of the Rydberg model, there should be a sharp transition to the disordered phase described by the condensation of the bosonic e anyons. Such a transition is not present in the QDMs, because the e excitations have been projected out by the dimer constraint. This QPT is in the universality class of the Ising* Wilson–Fisher conformal field theory (61–63) and can, in principle, be accessible in our system. However, we do not find clear-cut numerical evidence for it below, for our range of system sizes.

Extending the mapping from the Rydberg model to the QDM further, in *SI Appendix, section III*, we compute the parameters in (δ, R_b) space where a QSL phase might be expected to exist for the Rydberg system based on the (previously known) regime of stability of the QDM spin liquid (50, 51). This calculation leads to an estimate of $(\delta = 2.981, R_b = 1.997)$, which places us within the liquid regime of our phase diagram.

The Liquid Regime

At moderately large values of the detuning, we find an intermediate correlated regime—designated by the red star in Fig. 1E—which lies in between two solid phases but resists categorization as either one. The nomenclature “liquid,” defined earlier, connotes that the Rydberg excitations form a dense state in which the blockade introduces significantly more correlations than in the disordered regime. Prompted by the considerations described in the previous section, we first attempt to uncover the existence of any phase transitions in the vicinity of this regime. To that end, we temporarily focus on a specific blockade radius, $R_b = 1.9$ (dotted white line in Fig. 1E), and look at variations of the ground-state properties along this one-dimensional cut.

The first such observable is the susceptibility, defined as the second derivative of the ground-state energy, E_0 , with respect to

the detuning; i.e., $\chi = -\partial^2 E_0 / \partial \delta^2$. On finite systems, the maxima of the susceptibility can often be used to identify possible QCPs, which are slightly shifted from their locations in the thermodynamic limit. In particular, for $R_b = 1.9$, χ is plotted in Fig. 5A, where a single peak in the response is visible at approximately $\delta = 2.9$. This susceptibility peak—which is recorded by the pink circles in Fig. 1E—is also reproduced in exact diagonalization calculations on a 48-site torus (SI Appendix, section IV).

A similar signature can be discerned in the quantum fidelity $|\langle \Psi_0(\delta) | \Psi_0(\delta + \varepsilon) \rangle|$ (64, 65), which measures the overlap between two ground-state wavefunctions Ψ_0 computed at parameters differing by ε . The fidelity serves as a useful tool in studying QPTs because, intuitively, it quantifies the similarity between two states, while QPTs are necessarily accompanied by an abrupt change in the structure of the ground-state wavefunction (66). Zooming in on a narrower window around the susceptibility peak, we evaluate the fidelity susceptibility (67), which, in its differential form, is given by

$$\mathcal{F} \equiv 2 \left[\frac{1 - |\langle \Psi_0(\delta) | \Psi_0(\delta + \varepsilon) \rangle|}{\varepsilon^2} \right]. \quad [4]$$

The fidelity susceptibility also displays a local maximum at $\delta \approx 2.9$, indicating some change in the nature of the ground state as we pass into the liquid regime. Unlike the QPTs into the ordered phases, the EE (Fig. 5C) does not drop as we cross this point but rather, continues to increase; however, its first derivative is nonmonotonic at $\delta \approx 2.9$. This suggests that the final liquid state is likely highly entangled and is not a simple symmetry-breaking ground state.

Given that we always work on cylinders of finite extent, we cannot exclude the possibility that the peaks in Fig. 5A and B are due to surface critical phenomena (68, 69) driven by a phase transition at the edge. Indeed, in Fig. 6A, which shows a profile of the liquid regime on a wide cylinder at $\delta = 3.50$, $R_b = 1.95$, we notice that the edges seek to precipitate the most compatible density-wave order at these fairly large values of the detuning. Nonetheless, the bulk resists any such ordering tendencies and the central region of the system remains visibly uniform, with only slight perturbations from the open boundaries. In fact, the bulk fails to order despite being at a detuning for which the system energetically favors a maximal (constrained) packing of Rydberg excitations, as is also evidenced by the nearby staggered and nematic phases above and below the liquid regime, respectively. It is perhaps worth noting that in one spatial dimension, the comparable regions lying between the different \mathbb{Z}_n -ordered states at large detuning are known to belong to a Luttinger liquid phase (70).

To eliminate end effects, it is often useful to first evaluate the ground-state energy per site for an infinitely long cylinder by subtracting the energies of finite cylinders of different lengths but with the same circumference (31, 35, 71, 72). Such a subtraction scheme cancels the leading-edge effects, leaving only the bulk energy of the larger system. In particular, this procedure enables us to quantify the influence of the boundaries on thermodynamic properties of the system such as the susceptibility. Using two cylinders of fixed width, an estimate of the bulk energy can be found by subtracting the energy of the smaller system from that of the larger. The (negative of the) second derivative of this quantity with respect to the detuning defines the bulk susceptibility χ_b —this gives us the susceptibility in the center of the cylinder with minimal edge effects. Fig. 6B presents the variation of χ_b with detuning at $R_b = 1.90$ for the YC6 family: We see that the local maximum of the susceptibility reported in Fig. 5A is still identifiable, but its precise location is shifted to slightly higher δ . Analogously, we study the bulk susceptibility for wider YC8 cylinders and find, once again, a distinct peak corresponding to the onset of the liquid regime. Although this peak persists

in a purely bulk observable, its magnitude is diminished: For example, the relative change between the local maximum and the minimum (shoulder) immediately adjacent to it on the right (left) differs by approximately a factor of 4 (10) between χ_b and χ for the YC8 cylinder. Hence, the behavior of the susceptibility could be indicative of an edge phase transition but whether this is accompanied by, or due to, a change in the bulk wavefunction is presently unclear.

Next, we investigate the properties of this liquid regime in more detail and demonstrate that—as preempted by its name—it does not possess any long-range density-wave order. This diagnosis of liquidity is best captured by the static structure factor. In stark contrast to Fig. 3, $S(\mathbf{q})$ is featureless within the liquid regime (Fig. 7A) with the spectral weight distributed evenly around the extended Brillouin zone.

This unordered nature is reflected in Fig. 7B, where we plot the order parameters characterizing the surrounding symmetry-broken states. The order parameters defined earlier are found to be nonzero in both the nematic and staggered phases but are smaller by an order of magnitude in the liquid regime; this is compatible with a vanishing $|\Phi|^2$ and M_Φ^2 in the thermodynamic limit. In the process, we also find that the transition from the nematic (staggered) phase to the liquid regime appears to be second order (first order), which is consistent with the expectations for the QPT into a \mathbb{Z}_2 QSL in the dimer models, as we have discussed in the previous section. We do not observe any signatures of a phase transition within the liquid regime.

Moreover, one can also define a correlation length from the structure factor as (73)

$$\xi(\mathbf{Q}, \mathbf{q}_{\min}) = \frac{1}{|\mathbf{q}_{\min}|} \sqrt{\frac{S(\mathbf{Q})}{S(\mathbf{Q} + \mathbf{q}_{\min})} - 1}, \quad [5]$$

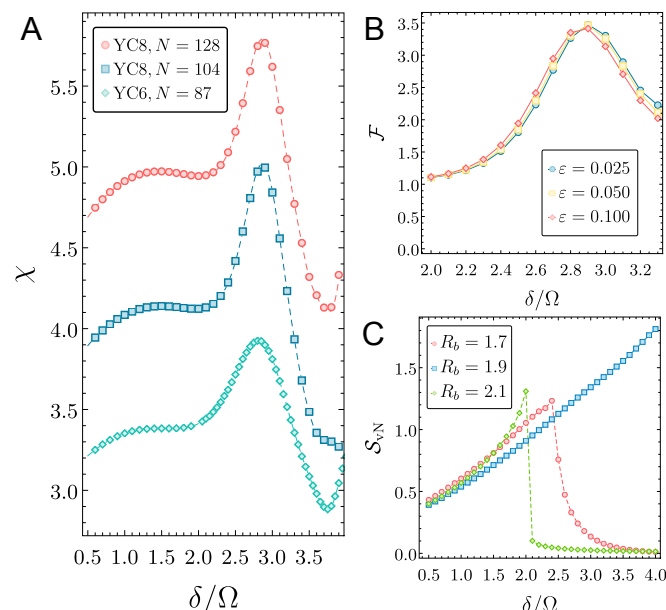


Fig. 5. Signatures of a crossover into the liquid regime. Along a line where the blockade radius is held constant at $R_b = 1.90$, both (A) the susceptibility χ and (B) the fidelity susceptibility \mathcal{F} exhibit a single peak at $\delta \approx 2.90$. (C) The behavior of the EE over the same detuning range, however, is distinct from the sharp drop observed across the QPTs into any of the ordered phases. On going to higher δ , the system eventually transitions into either the nematic or the string phase, depending on the blockade radius (or potentially the boundary conditions).

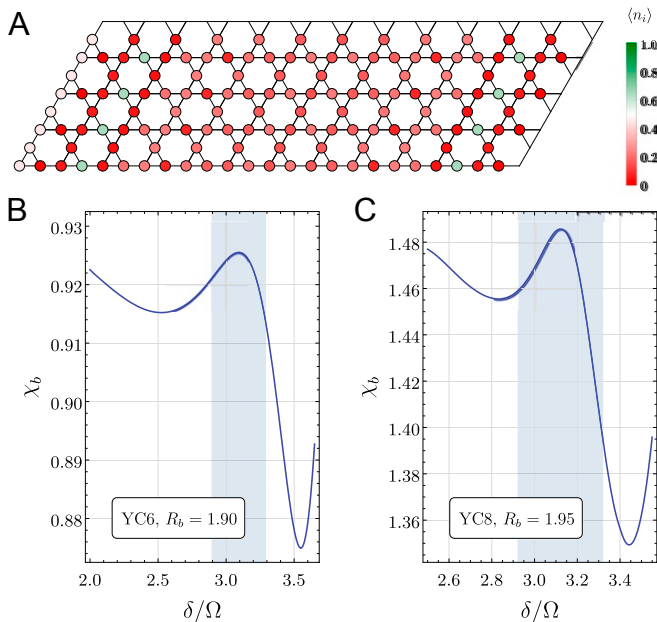


Fig. 6. Disentangling bulk and boundary behaviors. (A) Within the liquid regime—depicted here at $\delta = 3.50$, $R_b = 1.95$ —the real-space magnetization profile communicates the absence of density-wave order; note that the edge-induced ordering does not permeate into the bulk, which remains uniform. (B and C) Bulk susceptibilities: By construction, χ_b should be insensitive to edge effects. In B, χ_b is determined from the second derivative of the difference between the energies of two YC6 cylinders with lengths $N_1 = 12$ and $N_1 = 9$. As in Fig. 5A, with R_b set to 1.90, a clear local maximum appears at $\delta \approx 3.09$, heralding the liquid regime. On YC8 cylinders (C), the bulk susceptibility, shown here along $R_b = 1.95$, is calculated by applying the subtraction method to two systems of lengths $N_1 = 12$ and $N_1 = 8$.

where $\mathbf{Q} + \mathbf{q}_{\min}$ is the allowed wavevector immediately adjacent to the peak at \mathbf{Q} . The correlation lengths obtained in the liquid are found to be smaller than the lattice constant, as plotted in Fig. 7C, thus highlighting the lack of order. The qualitative behavior of ξ is the same along both directions on the cylinder and mirrors that of the order parameter. On either side of the liquid region, the correlation lengths follow an increasing trend as long-range order develops deep in the solid phases. We have further verified that the bond–bond correlation functions

$$C_{(i,j),(k,l)} = 4[\langle (n_i \cdot n_j)(n_k \cdot n_l) \rangle - \langle n_i \cdot n_j \rangle \langle n_k \cdot n_l \rangle] \quad [6]$$

are also short ranged in the liquid regime.

So far, our numerics point to a gapped (*SI Appendix*, Fig. S3), disordered candidate for the ground state of the liquid regime—these properties are all consistent with the behavior expected for a \mathbb{Z}_2 QSL, so it is natural to ask whether this region potentially harbors a topological phase. Although QSLs have long been fingerprinted by what the states are not, i.e., by the absence of ordering, more recently, it has been understood that the essential ingredient for a QSL is the presence of massive quantum superposition leading to an anomalously high degree of entanglement (12, 74). Accordingly, we search for positive indications of a QSL in the liquid regime by calculating the topological entanglement entropy (TEE) (75, 76) in *SI Appendix*, section II. For a QSL phase, the value of the TEE is universal and positive, representing a constant reduction to the area law entropy. Importantly, the TEE arises entirely from nonlocal entanglement and is topological in origin. While we do find indications of an enhanced long-range entanglement entropy (*SI Appendix*, Fig. S4), this does not serve as conclusive evidence for a \mathbb{Z}_2 QSL as a finite $\gamma \sim \ln 2$ has also been documented for a valence bond solid in a different model (71). Additionally, the TEE can suffer from strong finite-size effects on cylinders, leading to false signatures, and thus cannot always reliably distinguish between different quantum phases (77).

Discussion and Outlook

Based on numerical and theoretical analyses, we showed that the kagome lattice Rydberg atom array constitutes a promising platform for studying strongly correlated phenomena that supports not only a rich variety of quantum solids, but also, potentially, a highly entangled liquid regime. We argued that the liquid region could host a state corresponding to an elusive phase with topological order using its placement in the global phase diagram of triangular lattice quantum dimer models and theories of their quantum phase transitions. Our numerical study examined a number of signatures of the possible topological order and its associated phase transitions; although none of these computations conclusively confirm the existence of a topological phase for the available system sizes, they collectively point to interesting physics that merit further investigation.

This work can be extended in several directions. As the DMRG is neither an unbiased method nor free from finite-size effects, it would be worthwhile to more completely quantify these uncertainties in future theoretical works and definitively establish the nature of the liquid regime. A number of extensions to the present model can also be envisioned, e.g., by using various atom arrangements as well as multiple hyperfine sublevels or Rydberg atomic states to probe a variety of quantum entangled phases.

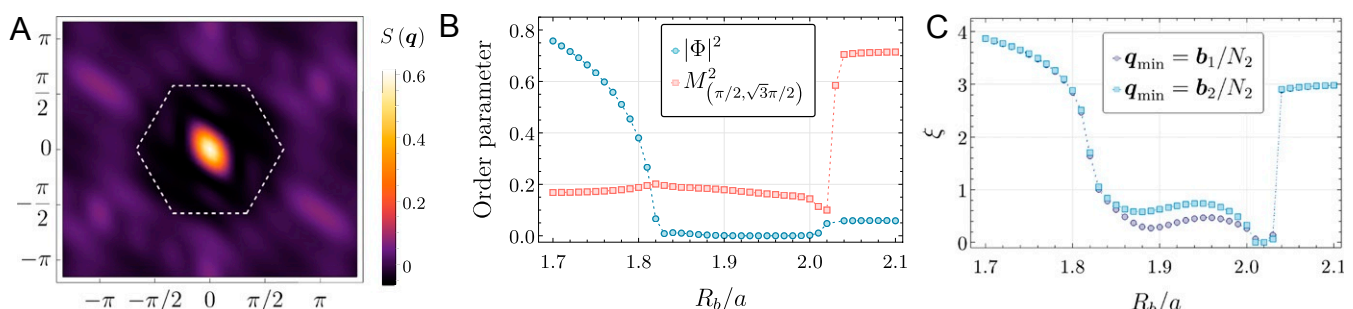


Fig. 7. Properties of the liquid regime. Here, we focus on the line $\delta = 3.3$ while varying the blockade radius. (A) The structure factor $S(\mathbf{q})$, at $R_b = 1.95$, is featureless with no discernible ordering peaks. (B) The order parameters $|\Phi|^2$ and M_0^2 characterizing the nematic and staggered phases, respectively. Both develop a clear trough in the liquid region between the two phases, indicating the lack of symmetry-breaking order therein. (C) The correlation lengths calculated from Eq. 3: For $1.9 \leq R_b \leq 2.0$, ξ is smaller than one lattice spacing, so all correlations are short ranged.

Furthermore, we expect the phase diagram in Fig. 1E to serve as a valuable guide to the detailed experimental studies of frustrated systems using Rydberg atom arrays. Specifically, both solid and liquid regimes can be reached starting from a trivial product ground state by adiabatically changing the laser detuning across the phase transitions, as was demonstrated previously (15). For experiments with $N \sim \mathcal{O}(10^2)$ Rb atoms coupled to a 70-S Rydberg state, the typical Rabi frequencies involved can be up to $(2\pi) \times 10$ MHz. With these driving parameters, sweeps over the detuning range $0 \leq \delta \lesssim 5 \Omega$, at interatomic spacings such that $R_b/a \lesssim 3.5$, have already been achieved in one-dimensional atom arrays (78–80). Hence, coherently preparing all of the different many-body ground states and observing their fundamental characteristics should be within experimental reach in two-dimensional systems as well (81, 82).

While the solid phases can be detected directly by evaluating the corresponding order parameter, the study of any possible QSL states in the liquid regime (or more generally, on Rydberg platforms) will require different approaches. In particular, measuring the statistics of microscopic state occupations (15) or the growth of correlations (18) across reversible QPTs could prove to be informative. In a Rydberg liquid, one can think of creating and manipulating topologically stable excitations, which cannot disappear except by pairwise annihilation with a partner excitation of the same type. The excitation types would correspond to the three nontrivial anyons of the \mathbb{Z}_2 spin liquid, and each should manifest as a characteristic local (and stable) “lump” in the density of atoms in the excited Rydberg state; interference experiments between such excitations could be used to scrutinize braiding statistics. The dynamic structure factor can also provide signatures of fractionalization: Dispersive

single-particle peaks will be observed in the disordered phase, while two-particle continua would appear in a region with \mathbb{Z}_2 topological order. Detailed study of such spectra could yield the pattern of symmetry fractionalization (48, 52, 83). Other directions include more direct measurements of the topological entanglement entropy (84, 85). Finally, classical and quantum machine-learning techniques (86–89) could be useful for measuring nonlocal topological order parameters associated with spin liquid states.

Materials and Methods

The DMRG calculations were performed using the iTensor Library (90). Further numerical details are presented in *SI Appendix, section I*.

Data Availability. All study data are included in this article and *SI Appendix*.

ACKNOWLEDGMENTS. We acknowledge useful discussions with Subhro Bhattacharjee, Meng Cheng, Yin-Chen He, Roger Melko, Roderich Moessner, William Witczak-Krempa, Ashvin Vishwanath, Norman Yao, and Michael Zaletel and especially the team of Dov Bluvstein, Sepehr Ebadi, Harry Levine, Ahmed Omran, Alexander Keesling, Giulia Semeghini, and Tout Wang. We are grateful to Marcus Bintz and Johannes Hauschild for pointing out the possibility of an edge transition and sharing their results. We also thank Adrian E. Feiguin for benchmarking the ground-state energies observed in our DMRG calculations. R.S. and S.S. were supported by the US Department of Energy under Grant DE-SC0019030. W.W.H., H.P., and M.D.L. were supported by the US Department of Energy under Grant DE-SC0021013, the Harvard-MIT Center for Ultracold Atoms, the Office of Naval Research, and the Vannevar Bush Faculty Fellowship. W.W.H. was additionally supported by the Gordon and Betty Moore Foundation’s Emerging Phenomena in Quantum Systems Initiative, Grant GBMF4306, and the National University of Singapore Development Grant AY2019/2020. The computations in this paper were run on the Faculty of Arts and Sciences Research Computing Cannon cluster supported by the Faculty of Arts and Sciences Division of Science Research Computing Group at Harvard University.

1. X. G. Wen, Colloquium: Zoo of quantum-topological phases of matter. *Rev. Mod. Phys.* **89**, 041004 (2017).
2. S. Sachdev, Topological order, emergent gauge fields, and Fermi surface reconstruction. *Rep. Prog. Phys.* **82**, 014001 (2019).
3. A. Y. Kitaev, Fault-tolerant quantum computation by anyons. *Ann. Phys.* **303**, 2–30 (2003).
4. H. L. Stormer, D. C. Tsui, A. C. Gossard, The fractional quantum Hall effect. *Rev. Mod. Phys.* **71**, S298–S305 (1999).
5. J. Nakamura, S. Liang, G. C. Gardner, M. J. Manfra, Direct observation of anyonic braiding statistics at the $\nu = 1/3$ fractional quantum Hall state. arXiv:2006.14115 (25 June 2020).
6. N. Read, S. Sachdev, Large- N expansion for frustrated quantum antiferromagnets. *Phys. Rev. Lett.* **66**, 1773–1776 (1991).
7. X. G. Wen, Mean-field theory of spin-liquid states with finite energy gap and topological orders. *Phys. Rev. B* **44**, 2664–2672 (1991).
8. T. H. Han et al., Fractionalized excitations in the spin-liquid state of a kagome-lattice antiferromagnet. *Nature* **492**, 406–410 (2012).
9. M. Fu, T. Imai, T. H. Han, Y. S. Lee, Evidence for a gapped spin-liquid ground state in a kagome Heisenberg antiferromagnet. *Science* **350**, 655–658 (2015).
10. Z. Feng et al., Gapped spin-1/2 spinon excitations in a new kagome quantum spin liquid compound $\text{Cu}_2\text{Zn}(\text{OH})_6\text{FBr}$. *Chin. Phys. Lett.* **34**, 077502 (2017).
11. L. Balents, Spin liquids in frustrated magnets. *Nature* **464**, 199–208 (2010).
12. L. Savary, L. Balents, Quantum spin liquids: A review. *Rep. Prog. Phys.* **80**, 016502 (2016).
13. H. Weimer, M. Müller, I. Lesanovsky, P. Zoller, H. P. Büchler, A Rydberg quantum simulator. *Nat. Phys.* **6**, 382–388 (2010).
14. H. Labuhn et al., Tunable two-dimensional arrays of single Rydberg atoms for realizing quantum Ising models. *Nature* **534**, 667–670 (2016).
15. H. Bernien et al., Probing many-body dynamics on a 51-atom quantum simulator. *Nature* **551**, 579–584 (2017).
16. R. Samajdar, S. Choi, H. Pichler, M. D. Lukin, S. Sachdev, Numerical study of the chiral \mathbb{Z}_3 quantum phase transition in one spatial dimension. *Phys. Rev. A* **98**, 023614 (2018).
17. S. Whitsitt, R. Samajdar, S. Sachdev, Quantum field theory for the chiral clock transition in one spatial dimension. *Phys. Rev. B* **98**, 205118 (2018).
18. A. Keesling et al., Quantum Kibble–Zurek mechanism and critical dynamics on a programmable Rydberg simulator. *Nature* **568**, 207–211 (2019).
19. R. Samajdar, W. W. Ho, H. Pichler, M. D. Lukin, S. Sachdev, Complex density wave orders and quantum phase transitions in a model of square-lattice Rydberg atom arrays. *Phys. Rev. Lett.* **124**, 103601 (2020).
20. S. de Léséleuc et al., Observation of a symmetry-protected topological phase of interacting bosons with Rydberg atoms. *Science* **365**, 775–780 (2019).
21. K. Roychowdhury, S. Bhattacharjee, F. Pollmann, \mathbb{Z}_2 topological liquid of hard-core bosons on a kagome lattice at 1/3 filling. *Phys. Rev. B* **92**, 075141 (2015).
22. M. C. Bañuls et al., Simulating lattice gauge theories within quantum technologies. *Eur. Phys. J. D* **74**, 165 (2020).
23. M. Saffman, T. G. Walker, K. Mølmer, Quantum information with Rydberg atoms. *Rev. Mod. Phys.* **82**, 2313–2363 (2010).
24. A. Browaeys, D. Barredo, T. Lahaye, Experimental investigations of dipole–dipole interactions between a few Rydberg atoms. *J. Phys. B Atom. Mol. Opt. Phys.* **49**, 152001 (2016).
25. D. Jaksch et al., Fast quantum gates for neutral atoms. *Phys. Rev. Lett.* **85**, 2208–2011 (2000).
26. M. D. Lukin et al., Dipole blockade and quantum information processing in mesoscopic atomic ensembles. *Phys. Rev. Lett.* **87**, 037901 (2001).
27. S. Sachdev, K. Sengupta, S. M. Girvin, Mott insulators in strong electric fields. *Phys. Rev. B* **66**, 075128 (2002).
28. S. R. White, Density matrix formulation for quantum renormalization groups. *Phys. Rev. Lett.* **69**, 2863–2866 (1992).
29. S. R. White, Density-matrix algorithms for quantum renormalization groups. *Phys. Rev. B* **48**, 10345–10356 (1993).
30. H. C. Jiang, Z. Y. Weng, D. N. Sheng, Density matrix renormalization group numerical study of the kagome antiferromagnet. *Phys. Rev. Lett.* **101**, 117203 (2008).
31. S. Yan, D. A. Huse, S. R. White, Spin-liquid ground state of the $S = 1/2$ kagome Heisenberg antiferromagnet. *Science* **332**, 1173–1176 (2011).
32. S. Depenbrock, I. P. McCulloch, U. Schollwöck, Nature of the spin-liquid ground state of the $S = 1/2$ Heisenberg model on the kagome lattice. *Phys. Rev. Lett.* **109**, 067201 (2012).
33. S. Liang, H. Pang, Approximate diagonalization using the density matrix renormalization-group method: A two-dimensional-systems perspective. *Phys. Rev. B* **49**, 9214–9217 (1994).
34. S. R. White, A. L. Chernyshev, Néel order in square and triangular lattice Heisenberg models. *Phys. Rev. Lett.* **99**, 127004 (2007).
35. E. M. Stoudenmire, S. R. White, Studying two-dimensional systems with the density matrix renormalization group. *Annu. Rev. Condens. Matter Phys.* **3**, 111–128 (2012).
36. P. Nikolić, T. Senthil, Theory of the kagome lattice Ising antiferromagnet in weak transverse fields. *Phys. Rev. B* **71**, 024401 (2005).
37. T. Pohl, E. Demler, M. D. Lukin, Dynamical crystallization in the dipole blockade of ultracold atoms. *Phys. Rev. Lett.* **104**, 043002 (2010).
38. S. Sachdev, *Quantum Phase Transitions* (Cambridge University Press, New York, NYC, 2011).
39. W. Janke, R. Villanova, Three-dimensional 3-state Potts model revisited with new techniques. *Nucl. Phys. B* **489**, 679–696 (1997).

40. H. C. Jiang, Z. Wang, L. Balents, Identifying topological order by entanglement entropy. *Nat. Phys.* **8**, 902–905 (2012).

41. D. Huerga, S. Capponi, J. Dukelsky, G. Ortiz, Staircase of crystal phases of hard-core bosons on the kagome lattice. *Phys. Rev. B* **94**, 165124 (2016).

42. R. Moessner, K. S. Raman, “Quantum Dimer Models” in *Introduction to Frustrated Magnetism*, C. Lacroix, P. Mendels, F. Mila, Eds. (Springer, Berlin, Heidelberg, Germany, 2011), pp. 437–479.

43. J. Villain, R. Bidaux, J. P. Carton, R. Conte, Order as an effect of disorder. *J. Phys. France* **41**, 1263–1272 (1980).

44. E. F. Shender, Antiferromagnetic garnets with fluctuationally interacting sublattices. *Sov. Phys. JETP* **56**, 178 (1982).

45. L. Balents, M. P. Fisher, S. M. Girvin, Fractionalization in an easy-axis Kagome antiferromagnet. *Phys. Rev. B* **65**, 224412 (2002).

46. S. V. Isakov, Y. B. Kim, A. Paramekanti, Spin-liquid phase in a spin-1/2 quantum magnet on the kagome lattice. *Phys. Rev. Lett.* **97**, 207204 (2006).

47. S. V. Isakov, M. B. Hastings, R. G. Melko, Topological entanglement entropy of a Bose-Hubbard spin liquid. *Nat. Phys.* **7**, 772–775 (2011).

48. G. Y. Sun *et al.*, Dynamical signature of symmetry fractionalization in frustrated magnets. *Phys. Rev. Lett.* **121**, 077201 (2018).

49. Y. C. Wang, M. Cheng, W. Witczak-Krempa, Z. Y. Meng, Fractionalized conductivity at topological phase transitions. arXiv:2005.07337 (15 May 2020).

50. R. Moessner, S. L. Sondhi, Resonating valence bond phase in the triangular lattice quantum dimer model. *Phys. Rev. Lett.* **86**, 1881–1884 (2001).

51. R. Moessner, S. L. Sondhi, Ising models of quantum frustration. *Phys. Rev. B* **63**, 224401 (2001).

52. Z. Yan, Y. C. Wang, N. Ma, Y. Qi, Z. Y. Meng, Triangular lattice quantum dimer model redux: Static and dynamic properties. arXiv:2007.11161 (30 July 2020).

53. R. A. Jalabert, S. Sachdev, Spontaneous alignment of frustrated bonds in an anisotropic, three-dimensional Ising model. *Phys. Rev. B* **44**, 686–690 (1991).

54. S. Sachdev, Kagome- and triangular-lattice Heisenberg antiferromagnets: Ordering from quantum fluctuations and quantum-disordered ground states with unconfined bosonic spinons. *Phys. Rev. B* **45**, 12377–12396 (1992).

55. S. Sachdev, M. Vojta, Translational symmetry breaking in two-dimensional antiferromagnets and superconductors. *J. Phys. Soc. Jpn. Suppl.* **B 69**, 1–9 (2000).

56. T. Senthil, M. P. A. Fisher, Z_2 gauge theory of electron fractionalization in strongly correlated systems. *Phys. Rev. B* **62**, 7850–7881 (2000).

57. R. Moessner, S. L. Sondhi, E. Fradkin, Short-ranged resonating valence bond physics, quantum dimer models, and Ising gauge theories. *Phys. Rev. B* **65**, 024504 (2002).

58. A. M. Essin, M. Hermele, Classifying fractionalization: Symmetry classification of gapped \mathbb{Z}_2 spin liquids in two dimensions. *Phys. Rev. B* **87**, 104406 (2013).

59. Y. Qi, L. Fu, Detecting crystal symmetry fractionalization from the ground state: Application to \mathbb{Z}_2 spin liquids on the kagome lattice. *Phys. Rev. B* **91**, 100401 (2015).

60. M. Zaletel, Y. M. Lu, A. Vishwanath, Measuring space-group symmetry fractionalization in \mathbb{Z}_2 spin liquids. *Phys. Rev. B* **96**, 195164 (2017).

61. A. V. Chubukov, T. Senthil, S. Sachdev, Universal magnetic properties of frustrated quantum antiferromagnets in two dimensions. *Phys. Rev. Lett.* **72**, 2089–2092 (1994).

62. M. Schuler, S. Whitsitt, L. P. Henry, S. Sachdev, A. M. Läuchli, Universal signatures of quantum critical points from finite-size torus spectra: A window into the operator content of higher-dimensional conformal field theories. *Phys. Rev. Lett.* **117**, 210401 (2016).

63. S. Whitsitt, S. Sachdev, Transition from the \mathbb{Z}_2 spin liquid to antiferromagnetic order: Spectrum on the torus. *Phys. Rev. B* **94**, 085134 (2016).

64. M. Cozzini, R. Ionicioiu, P. Zanardi, Quantum fidelity and quantum phase transitions in matrix product states. *Phys. Rev. B* **76**, 104420 (2007).

65. H. Q. Zhou, J. P. Barjaktarević, Fidelity and quantum phase transitions. *J. Phys. Math. Theor.* **41**, 412001 (2008).

66. S. J. Gu, Fidelity approach to quantum phase transitions. *Int. J. Mod. Phys. B* **24**, 4371–4458 (2010).

67. W. L. You, Y. W. Li, S. J. Gu, Fidelity, dynamic structure factor, and susceptibility in critical phenomena. *Phys. Rev. E* **76**, 022101 (2007).

68. K. Binder, D. P. Landau, Critical phenomena at surfaces. *Physica A* **163**, 17–30 (1990).

69. H. W. Diehl, The theory of boundary critical phenomena. *Int. J. Mod. Phys. B* **11**, 3503–3523 (1997).

70. P. Fendley, K. Sengupta, S. Sachdev, Competing density-wave orders in a one-dimensional hard-boson model. *Phys. Rev. B* **69**, 075106 (2004).

71. Z. Zhu, D. A. Huse, S. R. White, Weak plaquette valence bond order in the $S=1/2$ honeycomb J_1-J_2 Heisenberg model. *Phys. Rev. Lett.* **110**, 127205 (2013).

72. Z. Zhu, D. A. Huse, S. R. White, Unexpected z-direction Ising antiferromagnetic order in a frustrated spin-1/2 J_1-J_2 XY model on the honeycomb lattice. *Phys. Rev. Lett.* **111**, 257201 (2013).

73. A. W. Sandvik, Computational studies of quantum spin systems. *AIP Conf. Proc.* **1297**, 135–338 (2010).

74. T. Grover, Y. Zhang, A. Vishwanath, Entanglement entropy as a portal to the physics of quantum spin liquids. *New J. Phys.* **15**, 025002 (2013).

75. A. Kitaev, J. Preskill, Topological entanglement entropy. *Phys. Rev. Lett.* **96**, 110404 (2006).

76. M. Levin, X. G. Wen, Detecting topological order in a ground state wave function. *Phys. Rev. Lett.* **96**, 110405 (2006).

77. S. S. Gong, W. Zhu, D. N. Sheng, O. I. Motrunich, M. P. A. Fisher, Plaquette ordered phase and quantum phase diagram in the spin- $\frac{1}{2}$ J_1-J_2 square Heisenberg model. *Phys. Rev. Lett.* **113**, 027201 (2014).

78. M. Endres *et al.*, Atom-by-atom assembly of defect-free one-dimensional cold atom arrays. *Science* **354**, 1024–1027 (2016).

79. H. Levine *et al.*, High-fidelity control and entanglement of Rydberg-atom qubits. *Phys. Rev. Lett.* **121**, 123603 (2018).

80. A. Omran *et al.*, Generation and manipulation of Schrödinger cat states in Rydberg atom arrays. *Science* **365**, 570–574 (2019).

81. S. Ebadi *et al.*, Quantum Phases of Matter on a 256-Atom Programmable Quantum Simulator. arXiv:2012.12281 (22 December 2020).

82. P. Scholl *et al.*, Programmable quantum simulation of 2D antiferromagnets with hundreds of Rydberg atoms. arXiv:2012.12268 (22 December 2020).

83. J. Becker, S. Wessel, Diagnosing fractionalization from the spin dynamics of Z_2 spin liquids on the kagome lattice by quantum Monte Carlo simulations. *Phys. Rev. Lett.* **121**, 077202 (2018).

84. R. Islam *et al.*, Measuring entanglement entropy in a quantum many-body system. *Nature* **528**, 77–83 (2015).

85. T. Brydges *et al.*, Probing Rényi entanglement entropy via randomized measurements. *Science* **364**, 260–263 (2019).

86. D. L. Deng, X. Li, S. Das Sarma, Machine learning topological states. *Phys. Rev. B* **96**, 195145 (2017).

87. Y. Zhang, R. G. Melko, E. A. Kim, Machine learning \mathbb{Z}_2 quantum spin liquids with quasiparticle statistics. *Phys. Rev. B* **96**, 245119 (2017).

88. J. Carrasquilla, R. G. Melko, Machine learning phases of matter. *Nat. Phys.* **13**, 431–434 (2017).

89. I. Cong, S. Choi, M. D. Lukin, Quantum convolutional neural networks. *Nat. Phys.* **15**, 1273–1278 (2019).

90. M. Fishman, S. R. White, E. M. Stoudenmire, The ITensor software library for tensor network calculations. arXiv:2007.14822 (28 July 2020).